

Seasonal Variations of Seismic Travel-Time Changes in Binchuan, Southwestern China, Inferred from Large Volume Air-Gun Source Array Data

Yi Luan¹, Hongfeng Yang^{*1,2} , Baoshan Wang³ , Wei Yang⁴, Weitao Wang⁴, Jun Yang⁵, Xiaobin Li⁵, and Jiangjun Ran⁶ 

Abstract

Active sources, especially air-gun sources in the water reservoir, have proven to be powerful tools for detecting regional scale velocity changes. However, the water level change affects the repeatability of the air-gun waveform and, thus, affects the stability of the detection of the velocity changes. This article explores how to make full use of the air-gun signals excited at different water levels from analyzing three years of air-gun data recorded by 20 stations deployed from ~ 50 m to ~ 25 km from the source. At the same time, by utilizing the poroelastic model, we quantify both vertical and horizontal distances affected by the water level change. More important, supported by the strain data from one borehole strainmeter station, the influence mechanisms of the seasonal variation derived from the three years of air-gun data are also discussed. Results indicate the water level affects the main frequency of the air gun and has a strong influence on the coda wave. When the water level of the reservoir changes abruptly, the dominant effect on the derived delay time change is from the water level change. In this case, the deconvolution method can hardly eliminate the influence of the abrupt water level change. However, when the reservoir's water level changes gently, the delay time varies accordingly rather than inversely with the water level. Other reasons affect the material properties and, thus, influence the derived delay time. The modeled vertical component of poroelastic strain caused by the reservoir water level change is 1×10^{-7} . The observed strain (4×10^{-7}) from the strainmeter is likely associated with thermoelastic strain induced by temperature change. Our results show that although the long-term air-gun signal is affected by water level, there is still much information about changes in the subsurface that is worth mining.

Cite this article as Luan, Y., H. Yang, B. Wang, W. Yang, W. Wang, J. Yang, X. Li, and J. Ran (2023). Seasonal Variations of Seismic Travel-Time Changes in Binchuan, Southwestern China, Inferred from Large Volume Air-Gun Source Array Data, *Seismol. Res. Lett.* **94**, 1613–1626, doi: [10.1785/0220220200](https://doi.org/10.1785/0220220200).

[Supplemental Material](#)

Introduction

A variety of processes cause subsurface structural changes with time, including long-term tectonic stress build-up, short-term stress changes from seismic and volcanic processes (e.g., Schaff and Beroza, 2004; Brenguier *et al.*, 2008, 2014; Yang *et al.*, 2014), periodic changes caused by Earth tides (Reasenberg and Aki, 1974; Yamamura *et al.*, 2003; Takano *et al.*, 2014), and environmental reasons (Sens-Schönfelder and Wegler, 2006; Niu *et al.*, 2008; Meier *et al.*, 2010; Richter *et al.*, 2014). Because seismic velocity changes may provide reliable precursors to earthquakes and volcanic eruptions (Wegler *et al.*, 2006; Brenguier *et al.*, 2008; Niu *et al.*, 2008), the quantitative understanding and correction of the environmentally caused seismic velocity changes is very important to improve their detection ability (Wang *et al.*, 2017).

Because the quantitative comprehension of the crustal reaction to outside loadings is very crucial, various repeatable passive and active sources were applied in the detection of seismic velocity changes (Reasenberg and Aki, 1974; Yamamura *et al.*, 2003; Brenguier *et al.*, 2008; Niu *et al.*, 2008; Hillers *et al.*, 2015;

1. Earth and Environmental Sciences Programme, Faculty of Science, The Chinese University of Hong Kong, Shatin, Hong Kong, China,  <https://orcid.org/0000-0002-5925-6487> (HY); 2. Shenzhen Research Institute, The Chinese University of Hong Kong, Shenzhen, China; 3. School of Earth and Space Sciences, University of Science and Technology of China, Hefei, China,  <https://orcid.org/0000-0001-7203-9703> (BW); 4. Institute of Geophysics, China Earthquake Administration, Beijing, China; 5. Earthquake Agency of Yunnan Province, Kunming, China; 6. Department of Earth and Space Sciences, Southern University of Sciences and Technology, Shenzhen, China,  <https://orcid.org/0000-0001-9245-3346> (JR)

*Corresponding author: hyang@cuhk.edu.hk

© Seismological Society of America

Wang *et al.*, 2020). A large volume air-gun array has been proved to be a powerful tool to monitor seismic velocity changes (Reasenber and Aki, 1974; Chen *et al.*, 2007; Liu *et al.*, 2021; Yang *et al.*, 2021), especially in detecting daily velocity changes (Wang *et al.*, 2020; Luan *et al.*, 2022). However, studying seasonal variation with long-term air-gun signals is more challenging. The commonly studied environmental processes can strongly influence the seasonal changes in seismic velocities, such as temperature changes (Ben-Zion and Allam, 2013; Richter *et al.*, 2014), atmospheric pressure (Wang *et al.*, 2008), rainfall (Sens-Schönfelder and Wegler, 2006), and changes in the stress and strain due to alterations in the reservoir water level (Liu *et al.*, 2021) and groundwater level (Tsai, 2011; Yang *et al.*, 2018). More notably, the water level change affects the repeatability of the air-gun waveform and, thus, whether we can use the long-period air-gun data to detect the subsurface variations remains unknown (Liu *et al.*, 2021).

Based on the Binchuan Fixed Air-gun Signal Transmission Station (FASTS), an air-gun array was deployed in the Dayindian water reservoir in Binchuan, west Yunnan, China (Wang *et al.*, 2012). Liu *et al.* (2021) analyzed the influences of the reservoir water level change on the detection of air-gun seasonal travel-time changes in Binchuan, Yunnan, China. They found that the reservoir water level change affected the seismic travel-time changes of air-gun signals. Using nearly one-year air-gun data and ambient noise data in Binchuan, they concluded that the pattern of travel-time changes from the air-gun source differed from ambient noise. However, they did not quantify the effect of reservoir water level change on the repeatability of air-gun signals and the subsurface medium around the reservoir. The quantitative analysis of the influence of reservoir water level change is crucial, especially in deriving the subsurface structural variation from the repeated air-gun source.

Thus, we try to investigate the velocity changes and quantify the effect of reservoir water level change from analysis of three-year air-gun data from 2013 to 2015 in the same research area. Most previous studies did not compare the velocity change with records from strainmeter (Wang *et al.*, 2012, 2020; Liu *et al.*, 2021). The combination of using a repeatable air-gun source recorded by 20 stations with one borehole strainmeter is a remarkable coincidence, which enables us to investigate the temporal velocity changes in detail. In this study, we take advantage of signals excited at different water levels by introducing the deconvolution method to remove the impact of source change. Furthermore, we quantify the vertical and horizontal distances affected by the pore-pressure change from the poroelastic model. Subsequently, we report the observed seasonal velocity change and seasonal volumetric strain that occurs due to the thermal effect.

Study Region and Seismic Experiments

Utilizing the large-volume air-gun array, the world's first FASTS in land was built in the Binchuan basin, western

Yunnan, in April 2011 (Wang *et al.*, 2012). The region is tectonically active with numerous fault zones and frequent earthquakes (e.g., Jiang *et al.*, 2020, 2021; Yang *et al.*, 2020). The most recently notable one is the 2021 M_s 6.4 Yangbi earthquake that was preceded by a profound foreshock sequence, exhibiting a cascading rupture manner (e.g., Zhang *et al.*, 2022; Zhu *et al.*, 2022). Identifying subsurface changes during the earthquake preparation stage was one of the objectives to construct the FASTS in the region.

The air-gun array is positioned in the Dayindian reservoir (see Fig. 1a for array position; and Figs. S1 and S2, available in the supplemental material to this article, for the condition of the air-gun experiment), which is a 2 km² medium-size reservoir located on the Daying River, 7 km west of the Binchuan County, performing tasks such as flood control and irrigation. The air guns were placed 2 m underneath a 7 m² steel structure, which were towed 8 m below the water surface. The array was made up of four Bolt 1500LL air guns with firing pressure of 15 MPa, which are highly efficient for energy conversion and capable of generating highly repeatable signals (Chen *et al.*, 2014, 2017). The air-gun array was tested in 2011 and operating continuously since January 2013. The timing of air guns and the signal sampling in each receiver were accurately synchronized to the Global Positioning System (GPS) clock.

We selected 20 portable stations around the Binchuan seismic signal transmitting station (Fig. 1a). The nearest station CKT was deployed around 50 m from the source; the furthest station was at a distance of ~25 km from the source. Each station was equipped with a Güralp CMG-40T short-period sensor (frequency band from 2 s to 100 Hz) and a Reftek 130B datalogger (sampling rate of 100 data points per second). Most measurements were performed about 15 times every 24 hr from 10 p.m. to 5 a.m., during which the anthropogenic noise level is much lower (Song and Yang, 2022). Because of rainfall and the irrigation water used by the surrounding residents, the water level of the Dayindian reservoir changes to some extent (Fig. 1b,c). The water level of the reservoir was measured twice a day, once at 8 a.m. in the morning and once at 8 p.m. in the evening. In summer, the water level is below 5 m, which is not appropriate for air-gun excitation (Luan *et al.*, 2016). Thus, we lack data from day 129 to day 284. For various reasons, some shots are not recorded by all stations. The surface temperature, precipitation, and barometric pressure was likewise collected from the European Centre for Medium-Range Weather Forecasts, ECMWF, near the air-gun site.

A YRY-4 four-component borehole strainmeter is located in Yongsheng, about 121 km away from the air-gun source, which is not affected by the water level change of the Dayindian reservoir. The strainmeter is at a depth of 45 m (Chi, 2009). The instrument has a strain resolution of 10^{-10} . In YRY-4, the sum of two components of strain perpendicular to each other represents the volume strain (Chi, 2009).

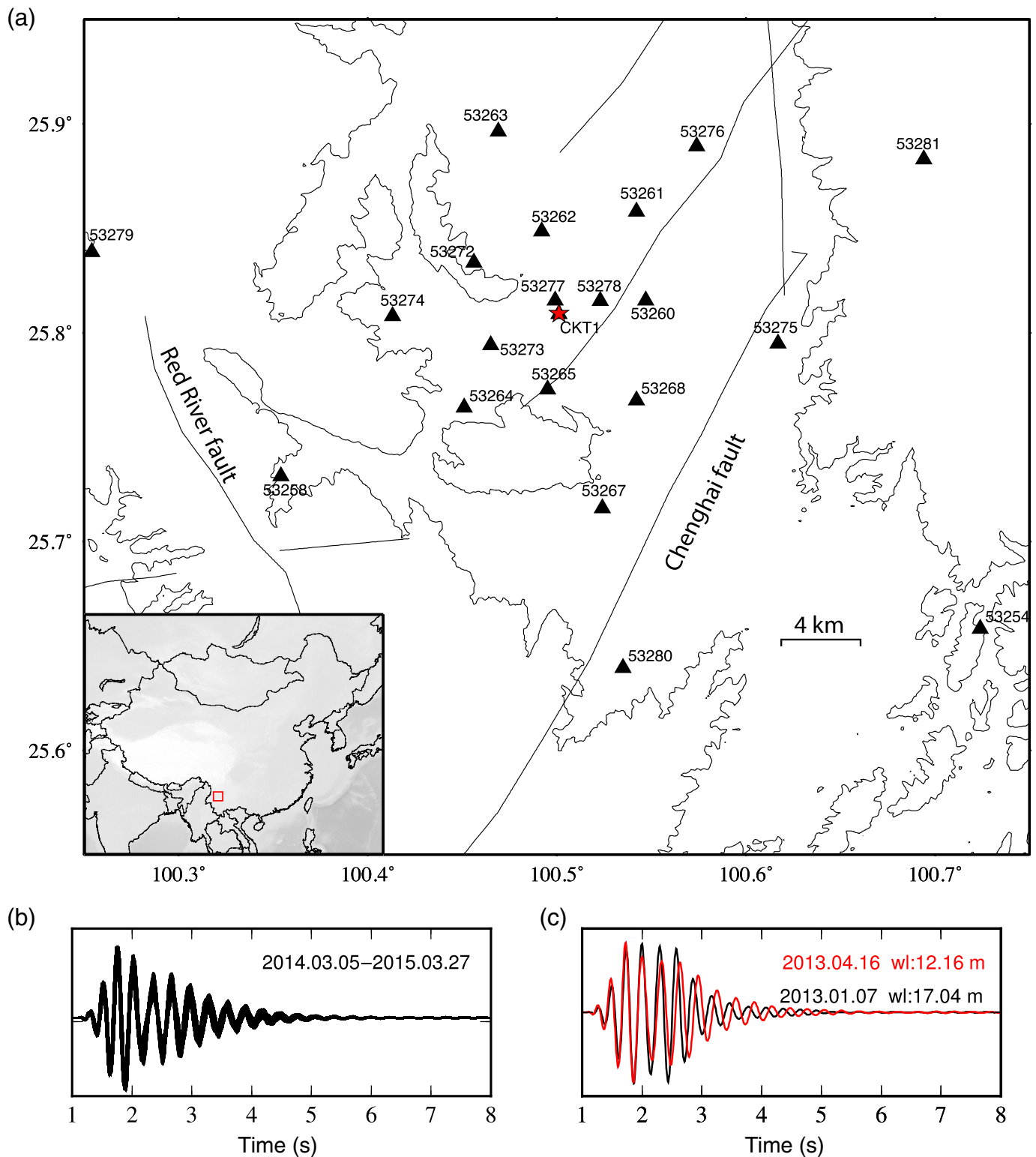


Figure 1. (a) Location of experiment site (red square) showing the air-gun source (red star) and stations (black triangle) used in this study. Cheng-hai fault and Red River fault are denoted by black lines. Lower inset figure shows tectonic setting in the region and the location (red box) of the study area. (b) Vertical component signals (band-pass filtered 3–5 Hz) recorded by the nearest CKT

station (~50 m) from 5 March 2014 to 27 February 2015. (c) Vertical component signal from two air-gun shots on 16 April 2013 with the water level of Dayindian reservoir at 12.16 m (red) and the signal on 7 January 2013 with a water level of 17.04 m. The color version of this figure is available only in the electronic edition.

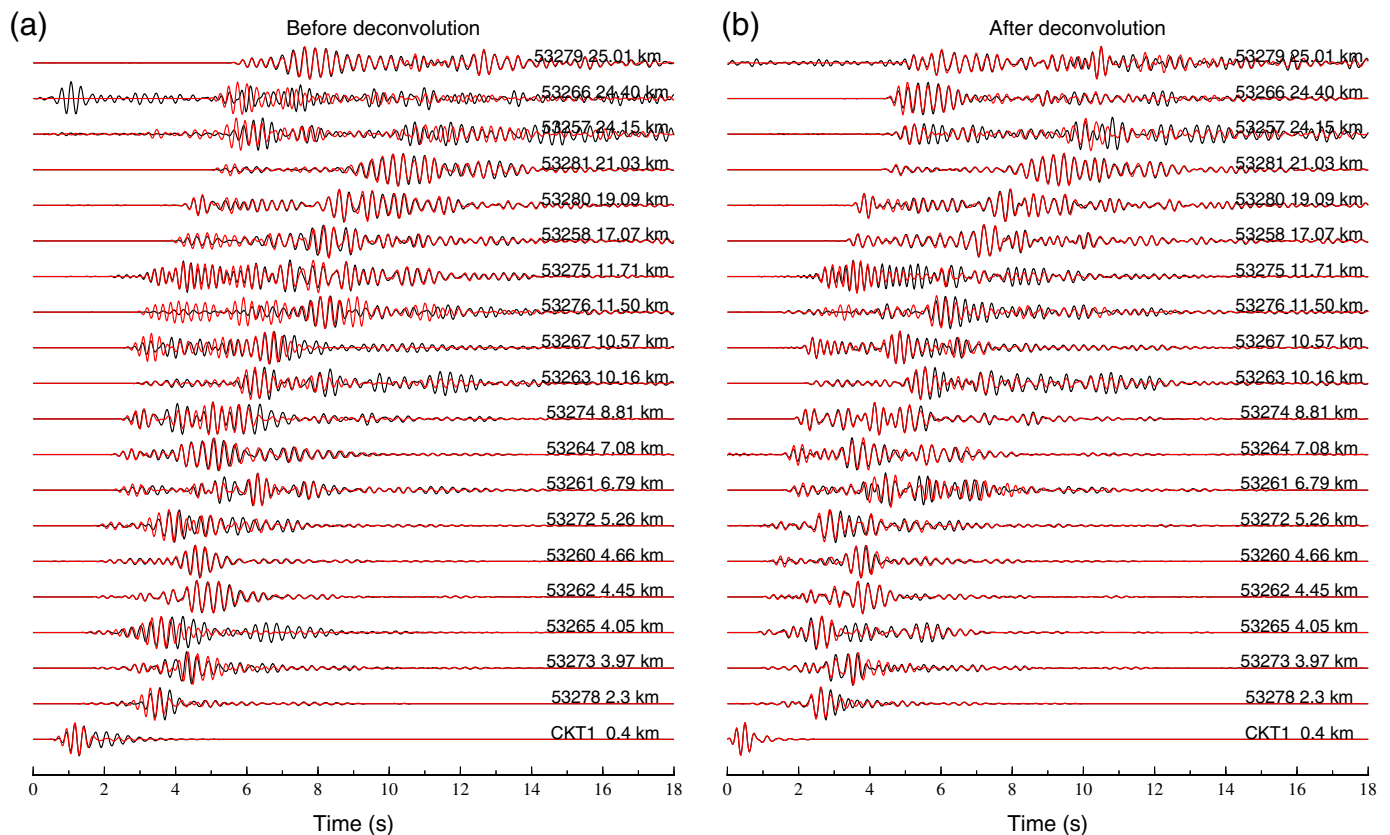


Figure 2. Pseudo record sections for (a) stacked air-gun signal in 2014 (red) and 2015 (black) and (b) stacked Green's function using deconvolution method in 2014 (red) and 2015 (black). The waveforms of all stations are band-pass filtered (3–5 Hz) vertical components. The Green's function eliminates time shifts between the waveforms compared to raw waveforms. The color version of this figure is available only in the electronic edition.

Methodology

Preprocessing

The air-gun excitation log records the excitation time from the GPS-synchronized process during each air-gun excitation. However, due to the influence of the gun control equipment, mechanical delay, time recording accuracy, and so forth, the recorded excitation and real excitation time in the gun control log exhibit a slight difference (Luan *et al.*, 2022). Therefore, we crop a 100 s air-gun signal of the nearest CKT station (~50 m from the air-gun source) and use it as the template. Then we apply the cross-correlation technique between the template and all the other signals of the CKT station to determine the relative air-gun excitation time. We can crop the 100 s signals recorded by other stations with the relative air-gun excitation time. All the cropped signals are de-averaged, detrend processed, and filtered by the 3–5 Hz Butterworth band-pass filter (Luan *et al.*, 2022). Because the source repeatability is quite high, the records are daily linear stacked to obtain an average signal.

Retrieving the Green's function

After preprocessing, the air-gun signals recorded by the nearest station are highly repeatable especially in the body wave part (Fig. 1b), and stacking them can produce excellent seismograms on stations both near and far from the source (Fig. 2a). However, a time shift caused by water level differences still exists, especially in the coda wave part (Figs. 1b and 2a).

Therefore, before we estimate the travel-time change (dt) in each station, we use a water-level deconvolution method to reduce the impact of delay time drift that does not stem from the real subsurface variation (Luan *et al.*, 2016, 2022; Wang *et al.*, 2020). The calculation method of the Fourier spectrum $G(\omega)$ of the Green's function is

$$G(\omega) = \frac{U(\omega)S^*(\omega)}{\max\{S(\omega)S^*(\omega)\}, C \max\{S(\omega)S^*(\omega)\}}, \quad (1)$$

in which $U(\omega)$ is the spectra of the far-field record, $S(\omega)$ is the spectra of the source signal, and $S^*(\omega)$ represents the complex conjugate. The water-level factor C is set as 0.0001. We choose the water-level deconvolution method because it has better computational efficiency compared with the time-domain iterative deconvolution method (e.g., Clayton and Wiggins, 1976; Ligorria and Ammon, 1999). The records of the nearest station CKT (offset ~50 m) are used as the source signals. The vertical

Green's functions are obtained by deconvolving the farther stations' signals with the source signals for every air-gun excitation (as Yang *et al.*, 2018; Wang *et al.*, 2020; Luan *et al.*, 2022). This procedure removes the influence of the source change (including air-gun fluctuating, working pressure fluctuating, etc.). The Green's functions from the remaining stations to the reference CKT station are obtained on an hourly basis. Because of the reproducibility of the source, we then combine all the vertical Green's functions of each station to provide a reference Green's function through the linear stacking method. Comparing the stacked seismograms for the years 2014 and 2015 (Fig. 2a) and the reference Green's function for the years 2014 and 2015 (Fig. 2b), we can see that subtle source changes shown because time shifts between the waveforms are eliminated to a certain extent through the deconvolution method.

Travel-time change measurement

We use the sliding window cross-correlation technique to extract the slight difference, dt , in the travel times of the waveforms from the two air-gun shots. The position of the cross-correlation function maxima between unperturbed and perturbed wavefields yields the value of dt (Snieder *et al.*, 2002; Wang *et al.*, 2008, 2020). The cosine interpolation of the calculation result is extracted to obtain the travel-time change (dt) with higher precision to improve the accuracy. When there is a change in the bulk velocity field, the travel-time change dt and the absolute travel time t will exhibit a linear relationship (e.g., Niu *et al.*, 2008; Snieder *et al.*, 2006). The relative velocity change, dv/v , is inverse to the slope of dt/t (i.e., $dv/v = -dt/t$).

The correlation coefficients and time shifts as a function of time are calculated by shifting a 0.3 s moving window from the first arrival time of the P wave. The 0.3 s moving window length was chosen because it approximated the length of a one-cycled waveform. The length of the time window was set to 1.0 s. We use the yearly stacked waveform as the reference when calculating the temporal travel-time variation (dt). All resulting temporal variations are measured between the reference and each daily stacked waveform in different stations. We focused on the travel-time changes (dt) of the first arrival and maximum amplitude of the vertical Green's function, which are regarded as P and S waves, respectively.

Results

We calculated the cross correlation between each daily stacked Green's function and the corresponding yearly stacked reference trace at station 53278 (offset ~ 2.32 km) (Fig. 3). The result yields high coherency in the P -wave (red box) and S -wave part (blue box) and large decoherence in the later coda-wave part. The correlation coefficients of the waveforms in the box are relatively high (>0.9) (Fig. 3c). For simplicity, we only plotted the waveforms of the year 2014 together with yearly stacked (red) and daily stacked (black) Green's function (Fig. 3b). The delay time of 3 yr of Green's function in the top is calculated using the red

box that is considered to be P wave, and the S wave in the blue box, respectively (Fig. 3a). The blank space shows the summer time with no air-gun excitation due to low water levels of the Dayindian reservoir (<5 m; Luan *et al.*, 2016). The P and S waves show the same trend in terms of the delay time. This confirms the robustness of the measured travel-time changes (dt). Furthermore, the delay time shows evident seasonal variations. On most days, the delay time of the P wave (red dots) changes is slightly stronger than that of the S wave (blue dots; e.g., 0–50 days). This indicates that the velocity changes of the P wave are stronger than the S wave velocity changes in station 53278 (offset ~ 2.3 km). This observation is consistent with the results from laboratory experiments, indicating that V_S is less sensitive to the effective stress than V_P , especially at shallow depths (Winkler and Liu, 2005; Wang *et al.*, 2020). The standard deviation of the measurements is 10^{-3} .

The periodic annual cycle dominates the delay time (Fig. 3a), which is visible on almost all stations (Fig. 4). The delay time of station 53278 decreases in January followed by a slight increase in February and a sharp increase in March. Such cycles repeat all the years from 2013 to 2015. Because of the lack of data, it is difficult for us to investigate the cycle in summer times. However, based on the data collected during the period August to December in 2014, we can clearly observe a slight decrease. Such decrease is consistent with the findings in the other two years even though with a shorter period. The delay time is remarkably similar at station 53278 (~ 2.32 km) and station 53262 (~ 4.45 km; Fig. 4a,c), indicating that the temporal changes of material properties are induced by similar factors. Because the location of station 53265 (offset ~ 4.05 km) is the nearest station to the Chenghai fault, the delay time of station 53265 behaves differently, and there is no apparent seasonal change (Fig. 4b). The differences in the delay time recorded by stations originate from the difference in rock property along the ray path. The rock property near the fault is generally characterized with high crack and high pore density. The delay time (or velocity changes) from the stations near the fault (e.g., station 53265) is stronger than the data observed in the mountain area. There is a sharp jump in the delay time in numerous stations starting from the 351th day in 2014 (black dashed line in Fig. 4). The background seismicity does not indicate that a large earthquake happened on that day. The precipitation or groundwater level changes are also unlikely to contribute to the sudden change in the observations. The sudden 2 m rise in the Dayindian water level (see Fig. 4; and Fig. S3) have caused an obvious change in the air-gun location, which resulted in the abrupt velocity change recorded by most stations. Although there are other sudden water level increases, they did not cause such impacts on the air-gun location and also on the delay time.

Discussion

The seasonal velocity changes may stem from two possible reasons. One is the changes in material properties. The other is the

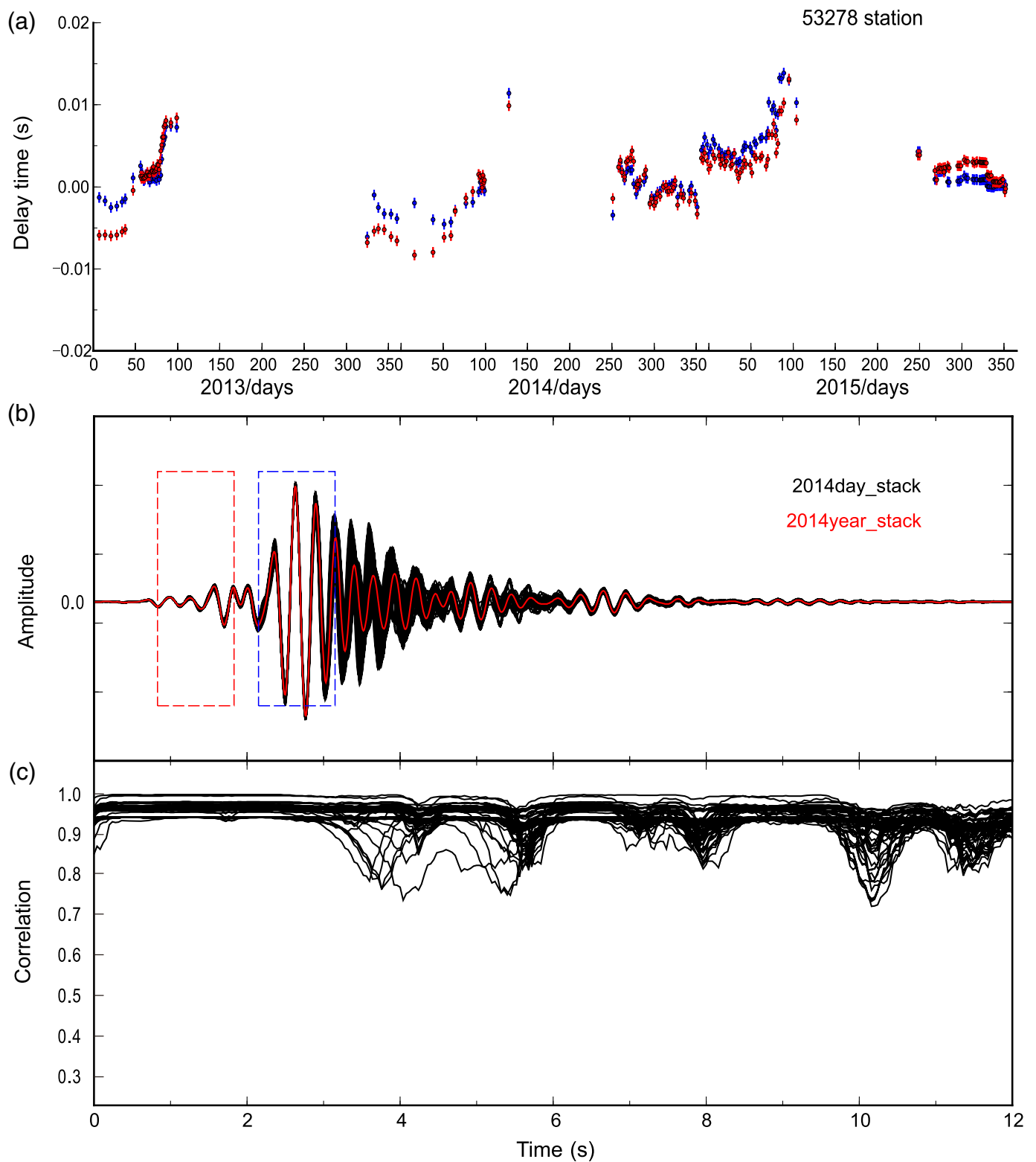
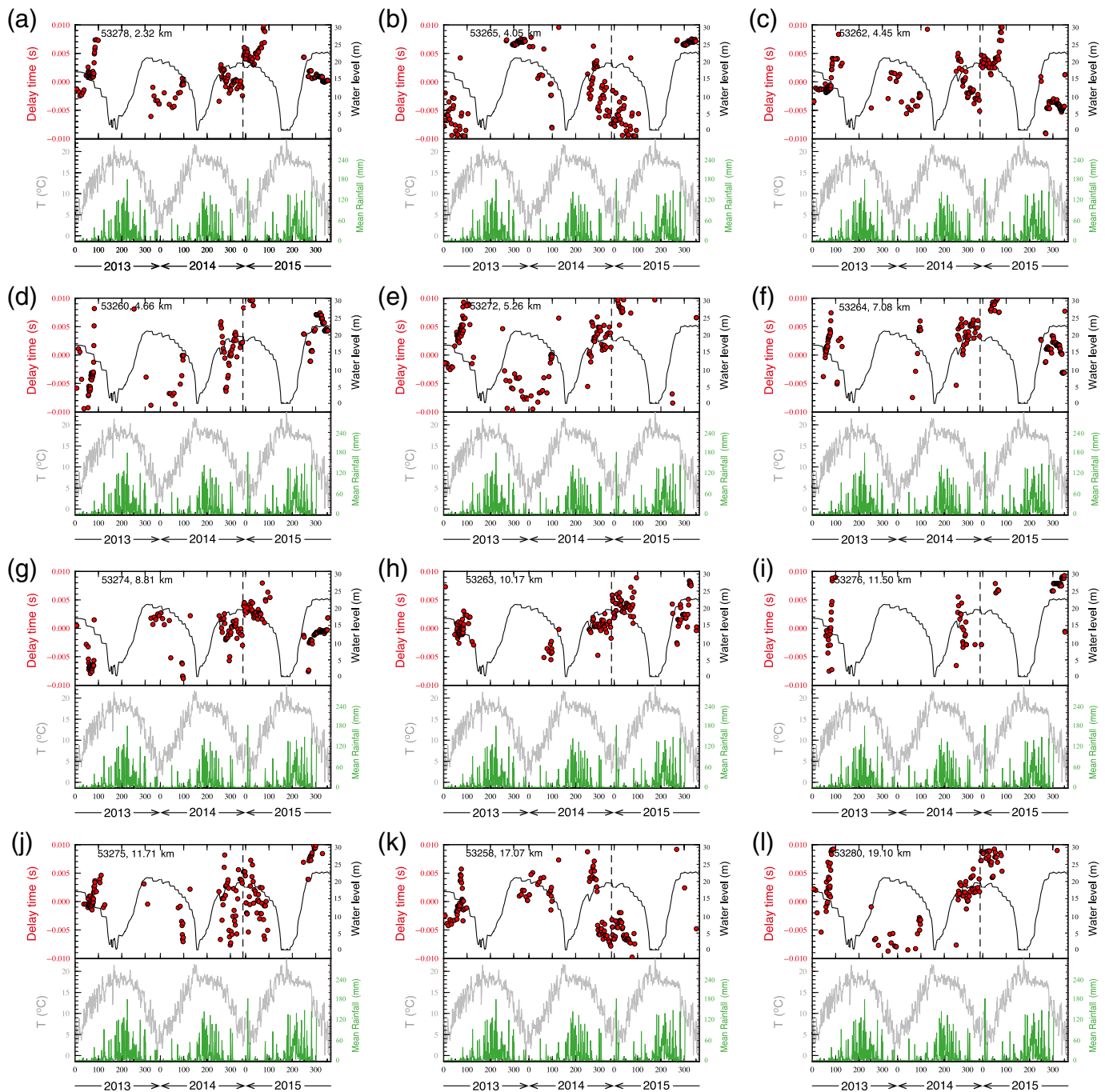


Figure 3. (a) Delay time (dt) of P wave (red) and S wave (blue) between linear stacked reference Green's function of year 2014 and daily stacked Green's function of 2014 at station 53278 (~ 2.3 km). (b) Band-pass filtered (3–5 Hz) vertical component reference Green's function (red) and daily stacked Green's

functions of 2014 (black). The red and blue rectangles indicate the time windows of P and S waves used to estimate the travel-time changes, respectively. (c) Correlation coefficient between and daily stacked Green's functions. The color version of this figure is available only in the electronic edition.



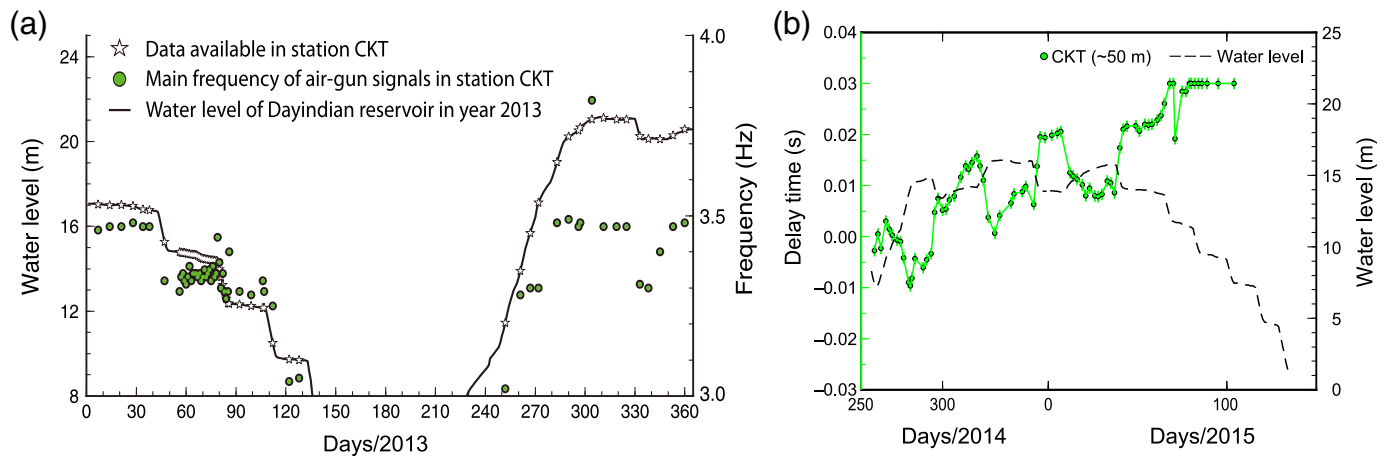
changes in source properties, including the air-gun source and wavefield properties near the source. We analyze the delay between the dt signal and the possible environmental data that exhibit seasonal changes to identify the dominant driving mechanism of the seasonal seismic velocity changes. These include the atmospheric temperature, precipitation, and the Dayindian reservoir water level records.

The effect of Dayindian reservoir water level change on the air-gun signal

Reservoir impoundment and discharge cause changes in the water level, leading to alterations of source characteristics.

Figure 4. Delay time (dt) of S wave between the linear stacked reference Green's functions and daily stacked Green's functions in the years 2013, 2014, 2015 (red dots) at the selected stations. The delay time shows a sudden rise on the 351st day in 2014. There is a clear correlation between the delay time (red dots) and the temperature (gray curve), water level change of Dayindian reservoir (black curve) and the mean local rainfall (green curve). The color version of this figure is available only in the electronic edition.

In 2013, the water level could reach 20 m in the winter and less than 8 m in summer (black line in Fig. 5a). The main frequency stemmed from the daily stacked signals recorded by the



reference CKT station (~ 50 m; hollow star in Fig. 5a). Changes in the water level will cause changes in the main frequency of the signal (green dots in Fig. 5a). Because the reservoir water level rises, the dominant frequency of the air-gun signal also increases. The delay time dt from the vertical component seismogram of the CKT station (~ 50 m) is most sensitive to changes in the water level of the Dayindian reservoir (Fig. 5b). Up to ~ 0.01 s delay changes in the later coda wave (5–6 s window) of the CKT station can be solely generated by the changes of Dayindian water level. The delay time is inversely proportional to the Dayindian water level change, except for the first observation in the delay time in 2014. We believe this one might be an outlier.

When the water level of the reservoir changes gradually (e.g., the water level of the Dayindian reservoir dropped 8 m within the first 120 days in the year 2013 with obvious increasing or decreasing trend; Fig. 5a), the dominant effect is the frequency and amplitude changes in the air-gun signal (Liu *et al.*, 2021), thus influencing the derived delay time between the air-gun waveforms. One crucial question is how far can the water level change affect. Liu *et al.* (2021) found that nearly all stations where apparent travel-time changes can be observed are mainly affected by the changes in the reservoir water level. Similar to what we observed in the CKT station, the delay time in farther away stations also shows an inverse trend compared to the water level change (Fig. 4). In this case, the deconvolution method can hardly eliminate the influence of the abrupt water level change.

However, when the water level of the reservoir changes gently (a slight change of water level within ~ 3 m over ~ 120 days and it shows nearly zero trend during the period; e.g., the water level of the Dayindian reservoir oscillates within 3 m between the wintertime of 2014 and the springtime of 2015), the delay time changes differently with the water level before and after the deconvolution method is applied (Figs. 4 and 5b). The delay time result of the CKT station is without applying the deconvolution method. The delay time changes inversely with the water level (Fig. 5b; and Fig. S4). For the gentle change type,

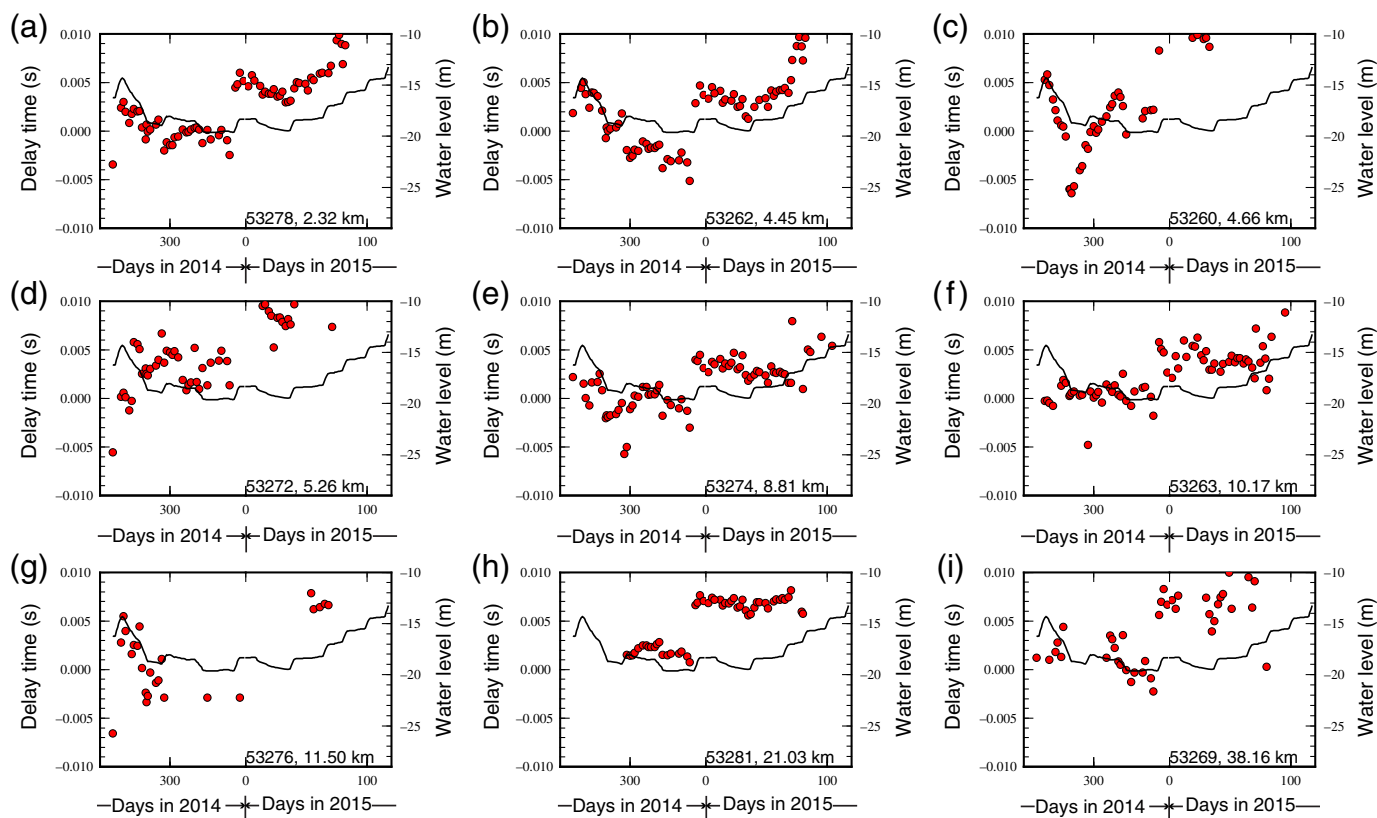
Figure 5. (a) Main frequency of the air-gun signal recorded by the CKT station (green dots) changes with the water level of Dayindian reservoir (black line). Days with air-gun excitation are marked with hollow stars. (b) Delay time (dt) of S -coda wave (5 and 6 s window after the picked arrival time with 1 s length) between the linear stacked reference raw waveform and daily stacked raw waveforms of years 2014, 2015 (green dots) at the reference CKT station (~ 50 m). There is a clear correlation between water level change of Dayindian reservoir (black dashed curve) and the delay time (green curve). The color version of this figure is available only in the electronic edition.

we calculated the correlation coefficient between the delay time and the water level change, which is -0.8 , indicating a highly inverse relation (see Fig. S4a). Furthermore, we applied a high-pass filter to both the delay time and the water level data to better emphasize their inverse relation (see Fig. S4c). For the gradual change type, the inverse correlation between the delay time and the water level change is even higher, that is, -0.9 (see Fig. S4b). In addition, we applied a running mean method to both the delay time and the water level data. One can clearly find that the delay time is inversely correlated with the water level (see Fig. S4d).

In contrast, the delay time of the farther stations changes after using the deconvolution method changes accordingly with the water level (Fig. 6). This phenomenon indicates that the deconvolution can, to some extent, reduce the influence of the water level change to secondary governing reasons. Apart from water level changes affecting the air-gun signal (the source), other reasons affect the material properties, and thus influence the derived delay time.

The poroelastic effect from Dayindian reservoir water level change

According to $dv/v = -dt/t$, the velocity change is inverse with the water level change when the water level changes gently (the wintertime of 2014 to the spring time of 2015; Fig. 6). The inverse relation between velocity change and the Dayindian



water level change is similar to the result found by Sens-Schönfelder and Wegler (2006) and Mordret *et al.* (2016). In Mordret *et al.* (2016), the increase of ground water level (the subsurface fluid distribution, not the reservoir water level in our study) from precipitation was found to increase the pore pressure and reopen the pores, leading to a seismic velocity decrease. Thus, the dominant contributors to the seasonality of most stations are probable poroelastic effect (Fig. 6).

We adopt the finite-element software (COMOSL Multiphysics) to simulate the poroelastic strain change caused by water level change. In this way, we can quantify the depth and horizontal distance affected by the pore-pressure change and determine whether the stations with different offsets can be influenced with a significant value. The poroelasticity describes the fluid flow in an elastic porous solid governed by mass conservation and Darcy's law. The governing equation is:

$$\frac{\partial(\rho\phi)}{\partial t} + \nabla \cdot \rho \left[\frac{-k}{\mu} (\nabla p + \rho g z) \right] = Q_m, \quad (2)$$

in which ρ is the fluid density, ϕ is the porosity, k is the permeability, μ is the viscosity, p is the pore pressure, g is the magnitude of gravitational acceleration, z is the vertical coordinate, and Q_m is the mass source. The strain amplitude is calculated with parameters listed in Table 1.

Assuming the shape of the reservoir is a square of 2 km by 2 km (see Fig. S5 for the 2D geometric model for the water

Figure 6. Delay time (dt) of S wave between the linear stacked reference Green's functions and daily stacked Green's functions of years 2014, 2015 (red dots) at the selected stations for which the delay time shows a sudden rise on the 351st day, 2014. There is an ~ 2 m water level rise corresponding to the sudden increase of delay time at the time of the 351st day in 2014. The color version of this figure is available only in the electronic edition.

reservoir load). The extreme example is that we set water level drops linearly from 15 to 0 m within 90 days and select the cross section of the reservoir to create a 2D model, with a uniformly distributed load of -1.5×10^5 Pa at the bottom of the reservoir with a water head of 15 m. Notably, the hydrologic effect in Tsai (2011) stems from the groundwater table, in which the pore pressure is set as $p_0 = 2.9 \times 10^4$ Pa, corresponding to a 3 m groundwater level change. Kalpna and Chander (2000) discussed the pore-pressure changes from the reservoir water load, indicating that the pore-pressure change of 5 kPa at the depth of 4.5 km was induced from a nearly 20 m reservoir water level change. Thus, the pore pressure induced by reservoir water level change in our case is far lower than that of the poroelastic model in Tsai (2011).

The water level change will cause temporal changes of subsurface medium near the source region. As shown in Figure 7, this also affects the temporal changes along the wavepath, especially within ~ 4 km, which could be recorded by all stations through the poroelastic effect. Usually, there is a phase delay

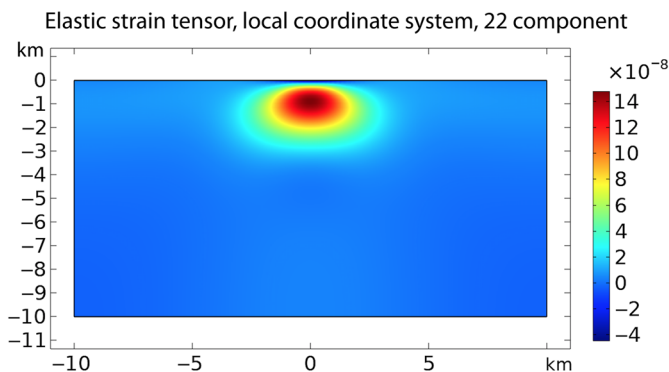


Figure 7. The simulation results of the water reservoir loading process. The vertical strain caused by a water level decrease of 15 m at $t = 90$ days is shown in different colors. The color version of this figure is available only in the electronic edition.

between the velocity change and the water level change. Tsai (2011) found that the dominant parameter influencing the phase lag for the poroelastic solution is the hydraulic diffusivity. The phase lag time between measured velocity change and reservoir water level change depends on the diffusion of water and pore pressure from the reservoir to the station (Luzón *et al.*, 2010). As discussed by Kalpna and Chander (2000), the total pore pressure induced at 4.5 km depth follows with the water level with a phase lag of 30–40 days.

If the poroelastic effect from the water level change represents the dominant contribution, the delay time of three stations with ~ 2.3 , ~ 4.5 , and ~ 21 km distance away from the reservoir will experience a different phase lag compared to the water level change, which is not found in our observation (Fig. 8). Other factors that have uniform coverage of the stations within 20 km may explain the consistency of the observed temporal changes.

Rainfall

The rainfall takes effect through direct loading or pore-pressure change. The latter poroelastic effect can extend to much greater depths (Tsai, 2011). The direct loading either increases or decreases the seismic velocity, depending on the medium property, such as the direction of the loading could open or close the underlying cracks (Li *et al.*, 2021). However, increase in the pore pressure from the infiltration of rainfall tends to decrease the seismic velocity (Mordret *et al.*, 2016).

The mean daily rainfall can hardly exceed 20 cm in our research area, and the rainfall data show apparent seasonal variations, with a peak in summer and a trough in winter (Fig. 4). However, there is no air-gun observation during summertime. The air-gun excitation focuses on wintertime with sparse rainfall. Thus, it is hard to determine whether there is a phase correlation between the travel-time change (dt) and the rainfall data. Liu *et al.* (2021) found that the seismic travel-time

TABLE 1

Model Parameters for the Poroelasticity

Reservoir Parameters	Values
Poisson's ratio	0.25
Porosity	0.1
Density of the rock	2300 kg/m ³
Permeability	10 ⁻¹⁴ m ²
Young's modulus	50 GPa
Biot–Willis coefficient	0.9

changes from the ambient noise data do not obviously correlate to the local rainfall but were induced by the poroelastic effect from the precipitation and evaporation. The travel-time changes (dt) lag behind the precipitation for about one month. In our case, the delay time changes (dt) in most stations show consistent variation (Fig. 4); we suggest that the seasonal delay time changes are not governed by the rainfall either through direct loading or poroelastic effect. The relationship between the delay time changes and the rainfall is still open and requires further investigation.

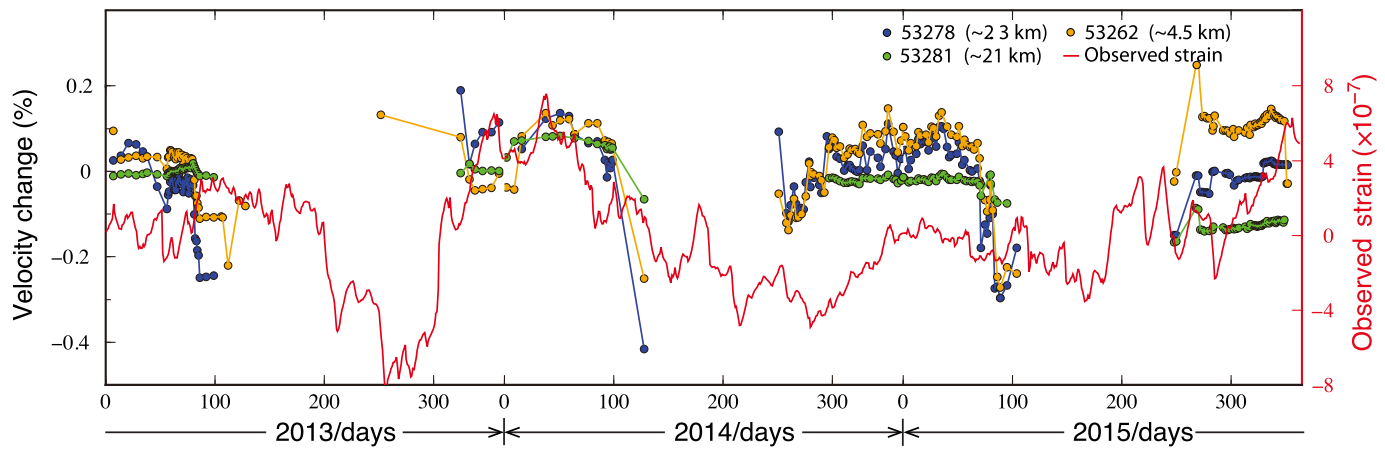
The thermoelastic effect

The temperature has always been viewed as a mechanism for seasonal velocity changes through the thermoelastic effect (Ben-Zion and Leary, 1986; Richter *et al.*, 2014; Luan *et al.*, 2022). As summarized by Ben-Zion and Allam (2013) and Tsai (2011), the thermoelastic strain induced by temperature change has an ~ 2 months' delay with temperature. Upon introducing an unconsolidated upper layer, the delay will become larger.

In our research area, the borehole strainmeter located in Yongsheng with three years' observed volume strain is shown as the red curve in Figure 8. The annual half-space strain recorded by the Yongsheng strainmeter is delayed about 100 days with the corresponding surface temperature signal. We shift the observed strain curve and the observed temperature curve by different time windows (the step is 10 days). When it reaches around 100 days, the correlation coefficient reaches the maximum value. Using the method of Ben-Zion and Leary (1986) and Tsai (2011), the 100 days' delay between the observed strain and the thermoelastic strain would indicate about 2 m of an unconsolidated upper layer (y_b) at that location. The thickness of y_b is given by

$$y_b = 2 \times \Delta t \sqrt{\pi \kappa / \tau}, \quad (3)$$

in which Δt is the delay between the observed strain and the thermoelastic strain, κ is the thermal diffusivity, τ is the annual period, $\tau = 365$.



We continue by evaluating the temperature-induced thermoelastic strain using the simplified equation by Tsai (2011)

$$\epsilon_{xx}(x,y,t) \approx A(t) \sin kx \times e^{-ky} [2(1-\nu) - ky], \quad (4)$$

$$\epsilon_{yy}(x,y,t) \approx -A(t) \sin kx \times e^{-ky} [2\nu - ky]. \quad (5)$$

The amplitude $A(t)$ is given by

$$A(t) = \frac{1+\nu}{1-\nu} k \alpha_{th} T_0 \sqrt{\frac{\kappa}{\omega}} e^{-\sqrt{\frac{\omega}{2\kappa}} y_b} \cos\left(\omega t - \sqrt{\frac{\omega}{2\kappa}} y_b - \frac{\pi}{4}\right), \quad (6)$$

in which ν is the Poisson's ratio, α_{th} is the thermal expansion coefficient, κ is the thermal diffusivity, k is the horizontal wavenumber, and ω is the frequency. The values are given in Table 2.

We compare the observed strain with the velocity change recorded by three stations with source-receiver distance of 2.3, 4.5, and 21 km, respectively (Fig. 8). The step on the 351st day in 2014 caused by the water level change has been removed to focus on the thermal effect. The seasonal changes in the seismic velocity are on the order of $\sim 0.1\%$. Notably, apart from the velocity change on the 351st day in 2014, the general trend of velocity change is consistent with the observed strain data. Besides, there is little phase lag between the velocity changes of the three stations and the observed strain.

The observed temperature record exhibits an apparent seasonal variation (green curve in Fig. 9a), with ~ 100 days' delay compared to the observed strain data in Yongsheng station (red curve in Fig. 9a). We take the temperature variations at a depth of 2 m as the input source for calculating the thermoelastic strain amplitude (equation 5). Detailed information for the equation can be found in Tsai (2011). The predicted strain used to compare with the observed volume strain is the sum of the horizontal plane strain ϵ_{xx} and vertical strain ϵ_{yy} . In Figure 9b, after introducing the unconsolidated upper layer $y_b = 2$, the phase of the modeled thermoelastic strain agrees well with the observed strain. The amplitude of thermoelastic strain can contribute nearly 75% of the observed strain.

Figure 8. Three years of observed strain (red line) in borehole strainmeter in Yongsheng station (red line) and measured S -wave velocity change in station 53278 (~ 2.3 km), station 53262 (~ 4.5 km) and station 53281 (~ 21 km). The color version of this figure is available only in the electronic edition.

Tsai (2011) evaluated the velocity changes induced by thermoelastic strain using third-order elasticity theory of Murnaghan (1951) and argued that the thermoelastic effect was hard to explain the $\sim 0.2\%$ velocity change. However, because $\frac{\Delta v}{v}$ is the local velocity change rather than observed velocity change, we should compare $\int_r \frac{\Delta v}{v} dr$ (r is the whole wavepath) with the $\sim 0.2\%$ velocity change rather than $\frac{\Delta v}{v}$ itself (Luan et al., 2022), calculated from Murnaghan parameters. Indeed, the observed velocity change is comparable with the integral of $\frac{\Delta v}{v}$ over the whole wavepath induced by the thermoelastic strain (Richter et al., 2014). Luan et al. (2022) also confirmed their observed annual and daily seismic velocity changes with the thermoelastic stress. The thermoelastic stress and strain induced by surface temperature changes with annual cycle are calculated using the method in Richter et al. (2014).

TABLE 2
Model Parameters for the Thermoelastic Strain

Reservoir Parameters	Symbol	Values
Poisson's ratio	ν	0.25
Angular frequency	ω	$2 \times 10^{-7} \text{ s}^{-1}$
Temperature amplitude	T_0	2.5°C
Wavenumber	k	$2\pi/10 \text{ km}$
Linear thermal expansion	α	$10^{-5} \text{ }^\circ\text{C}^{-1}$
Thermal diffusivity	κ	$10^{-6} \text{ m}^2/\text{s}$

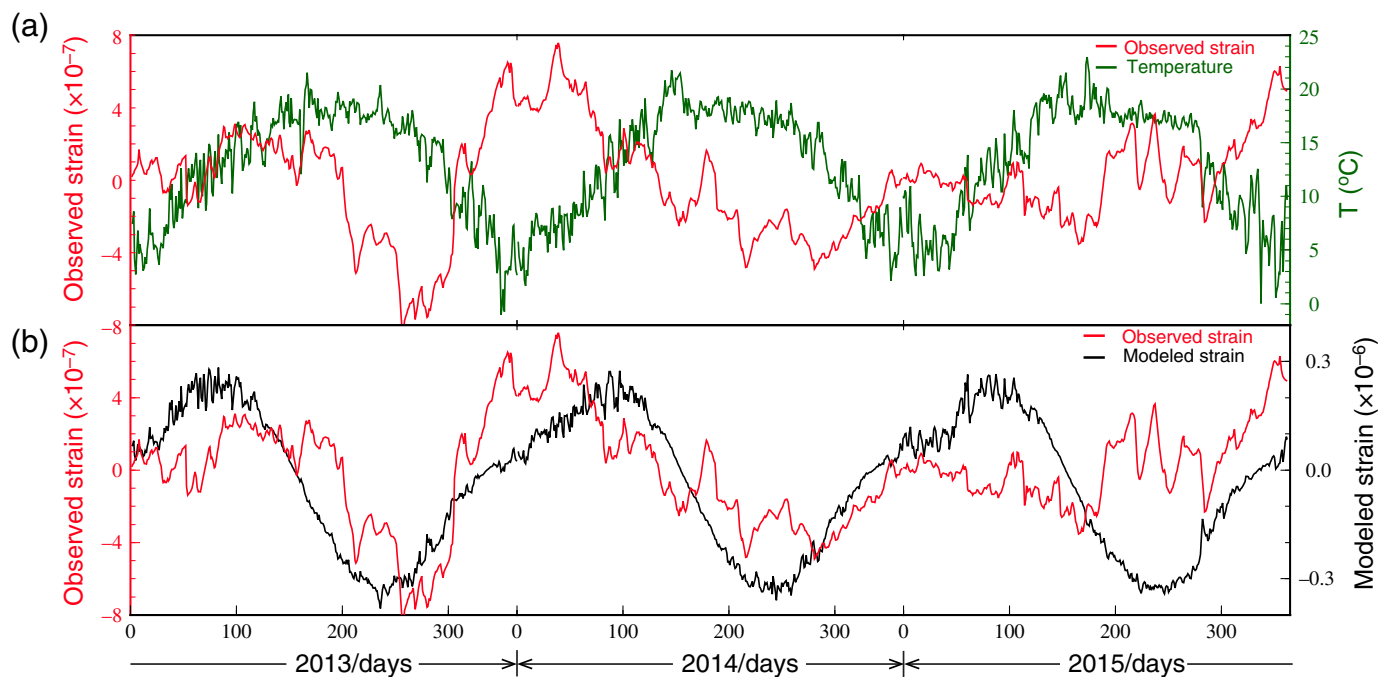


Figure 9. (a) Three years of observed strain (red line) and observed surface mean temperature time series (green line) at Yongsheng station. (b) Observed strain (red line) and model predicted strain (black line). The color version of this figure is available only in the electronic edition.

Conclusions

The travel-time (dt) changes from P and S wave from 3 yr of air-gun data in the Binchuan area shows significant seasonal variations. The phases of the seasonal variations recorded by different stations have remarkably consistent patterns. Quantitative analysis of the environmental influence will help us build a better model for the correction of seasonal effects.

Our results suggest that the water level change causes waveform distortion and induces a main frequency change in the air-gun signal. However, the water level affects the measured delay time in two ways. When the water level of the reservoir changes abruptly, the dominant effect on the derived delay time change is from the water level change. We observed that the delay time correlates inversely to the water level change. In this case, the deconvolution method can hardly eliminate the influence of the abrupt water level change. When the reservoir's water level changes gently, the delay time varies accordingly with the water level through the poroelastic effect. The phases of delay time also correlate to the temperature change. We compared the impact of the poroelastic effect and the influence of the thermoelastic effect. The thermoelastic effect from temperature change appears to be the most reasonable cause of the seasonality. The general trend of the velocity change at stations farther away is consistent with the observed strain data, which is dominated by the thermoelastic strain. The observed velocity change is comparable with the integral of the local velocity change over the entire wavepath induced by the thermoelastic strain.

Our study shows that although the long-term air-gun signal is affected by water level, there is still much information about changes in the subsurface that is worth mining. The analysis of the travel-time changes based on the air-gun data and the

driving forces, including reservoir water level change and atmospheric reasons, can provide insights to understand the mechanism of the seismic velocity changes in the subsurface. This also provides a better model for correcting seasonal effects, leading to a more precise estimation of seismic velocity change and an understanding of the variations in the subsurface structure.

Data and Resources

The seismic data used in this study were collected from the ChinArray Seismic Data Center available at <http://www.chinarraydmc.cn> (doi: 10.12001/ChinArray. Data). Data can also be obtained from the coauthor Baoshan Wang under request. The supplemental material includes five additional figures.

Declaration of Competing Interests

The authors acknowledge that there are no conflicts of interest recorded.

Acknowledgments

This work is supported by the National Science Foundation of China (Grant Numbers U2139203, 41974069, and 41974094), Hong Kong Synthetic Aperture Radar (SAR) Research Grant Council (Grant Number 14306122), National Key R&D Program of China (Grant Number 2018YFC1503400), and China Earthquake Science Experiment Project, CEA (Grant Number 2019CSES0107). The

NASA's Shuttle Radar Topography Mission (SRTM) topography data used in Figure 1 were downloaded from <https://www.usgs.gov/centers/eros> (last accessed December 2021). The other figures were prepared with Generic Mapping Tools (Wessel *et al.*, 2013). Figure S1 was prepared with Google Earth Pro V 7.3.6.9345; Dayindian reservoir: 25° 48' 19" N, 100° 29' 54" E, 1593 m, and the relevant information is available at <http://earth.google.com> (last accessed April 2022).

References

- Ben-Zion, Y., and A. A. Allam (2013). Seasonal thermoelastic strain and postseismic effects in Parkfield borehole dilatometers, *Earth Planet. Sci. Lett.* **379**, 120–126, doi: [10.1016/j.epsl.2013.08.024](https://doi.org/10.1016/j.epsl.2013.08.024).
- Ben-Zion, Y., and P. Leary (1986). Thermoelastic strain in a half-space covered by unconsolidated material, *Bull. Seismol. Soc. Am.* **76**, 1447–1460.
- Brenguier, F., M. Campillo, C. Hadziioannou, N. M. Shapiro, R. M. Nadeau, and E. Larose (2008). Postseismic relaxation along the San Andreas fault at Parkfield from continuous seismological observations, *Science* **321**, 1478–1481.
- Brenguier, F., M. Campillo, T. Takeda, Y. Aoki, N. M. Shapiro, X. Briand, K. Emoto, and H. Miyake (2014). Mapping pressurized volcanic fluids from induced crustal seismic velocity drops, *Science* **345**, no. 6192, 80–82.
- Chen, Y., B. S. Wang, and H. J. Yao (2017). Seismic airgun exploration of continental crust structures, *Sci. China Earth Sci.* **60**, no. 10, 1739–1751, doi: [10.1007/s11430-016-9096-6](https://doi.org/10.1007/s11430-016-9096-6).
- Chen, M., W. Yang, W. T. Wang, B. S. Wang, H. K. Ge, L. Chen, Y. S. Ding, J. Y. Qiao, and Y. Chen (2014). Influencing factors of seismic signals generated by un-tuned large volume airgun array in a land reservoir, *Earthq. Sci.* **27**, 365–376, doi: [10.1007/s11589-014-0073-0](https://doi.org/10.1007/s11589-014-0073-0).
- Chen, Y., X. K. Zhang, X. L. Qiu, H. K. Ge, B. J. Liu, and B. S. Wang (2007). A new way to generate seismic waves for continental crustal exploration, *Chin. Sci. Bull.* **52**, no. 16, 2264–2268, doi: [10.1007/s11434-007-0247-4](https://doi.org/10.1007/s11434-007-0247-4).
- Chi, S. (2009). China's component borehole strainmeter network, *Earthq. Sci.* **22**, 579–587, doi: [10.1007/s11589-009-0579-z](https://doi.org/10.1007/s11589-009-0579-z).
- Clayton, R., and R. Wiggins (1976). Source shape estimation and deconvolution of teleseismic body wave, *Geophys. J. Roy. Astron. Soc.* **47**, 151–177.
- Hillers, G., L. Retailleau, M. Campillo, A. Inbal, J. P. Ampuero, and T. Nishimura (2015). In situ observations of velocity changes in response to tidal deformation from analysis of the high-frequency ambient wavefield, *J. Geophys. Res.* **120**, doi: [10.1002/2014JB011318](https://doi.org/10.1002/2014JB011318).
- Jiang, X., S. Hu, and H. Yang (2021). Depth extent and V_p/V_s of the Chenghai fault zone, Yunnan, China constrained from dense-array-based teleseismic receiver functions, *J. Geophys. Res.* doi: [10.1029/2021JB022190](https://doi.org/10.1029/2021JB022190).
- Jiang, X., H. Yang, W. Yang, and W. Wang (2020). Crustal structure in the Binchuan region of Yunnan using receiver function with a 2-D seismic dense array, earthquake science, *Earthq. Sci.* **33**, 264–272, doi: [10.29382/eqs-2020-0264-01](https://doi.org/10.29382/eqs-2020-0264-01).
- Kalpna, , and R. Chander (2000). Green's function based stress diffusion solutions in the porous elastic half space for time varying finite reservoir loads, *Phys. Earth Planet. In.* **120**, 93–101, doi: [10.1016/S0031-9201\(00\)00146-1](https://doi.org/10.1016/S0031-9201(00)00146-1).
- Ligorria, J. P., and C. J. Ammon (1999). Iterative deconvolution and receiver-function estimation, *Bull. Seismol. Soc. Am.* **89**, 1395–1400.
- Li, J. W., D. X. Song, Y. Yang, M. K. Li, J. T. Li, and Y. Li (2021). Strong seasonal variations of seismic velocity in eastern margin of Tibetan Plateau and Sichuan Basin from ambient noise interferometry, *J. Geophys. Res.* **126**, e2021JB022600, doi: [10.1029/2021JB022600](https://doi.org/10.1029/2021JB022600).
- Liu, C. Y., H. F. Yang, B. S. Wang, and J. Yang (2021). Impacts of reservoir water level fluctuation on measuring seasonal seismic travel time changes in the Binchuan basin, Yunnan, China, *Remote Sens.* **13**, 2421, doi: [10.3390/rs13122421](https://doi.org/10.3390/rs13122421).
- Luan, Y., H. F. Yang, and B. S. Wang, (2016). Large volume air-gun waveform data processing (I): Binchuan, Yunnan, *Earthq. Res. China.* **2**, 305–318.
- Luan, Y., H. F. Yang, B. S. Wang, W. Yang, W. T. Wang, J. Yang, and X. B. Li (2022). Time-lapse monitoring of daily velocity changes in Binchuan, Southwestern China, using large-volume air-gun source array data, *Seismol. Res. Lett.* **93**, 914–930, doi: [10.1785/0220210160](https://doi.org/10.1785/0220210160).
- Luzón, F., A. García-Jerez, M. A. Santoyo, and F. J. Sánchez-Sesma (2010). Numerical modelling of pore pressure variations due to time varying loads using a hybrid technique: The case of the Itoiz reservoir (Northern Spain), *Geophys. J. Int.* **180**, 327–338, doi: [10.1111/j.1365-246X.2009.04408.x](https://doi.org/10.1111/j.1365-246X.2009.04408.x).
- Meier, U., N. M. Shapiro, and F. Brenguier (2010). Detecting seasonal variations in seismic velocities within Los Angeles basin from correlations of ambient seismic noise, *Geophys. J. Int.* **181**, 985–996, doi: [10.1111/j.1365-246X.2010.04550.x](https://doi.org/10.1111/j.1365-246X.2010.04550.x).
- Mordret, A., T. D. Mikesell, C. Harig, B. P. Lipovsky, and G. A. Prieto (2016). Monitoring southwest Greenland's ice sheet melt with ambient seismic noise, *Sci. Adv.* **2**, e1501538, doi: [10.1126/sciadv.1501538](https://doi.org/10.1126/sciadv.1501538).
- Murnaghan, F. D. (1951). *Finite Deformation of an Elastic Solid*, Wiley, New York.
- Niu, F. L., P. G. Silver, T. M. Daley, X. Cheng, and E. L. Majer (2008). Preseismic velocity changes observed from active source monitoring at the Parkfield SAFOD drill site, *Nature* **454**, 204–208.
- Reasenber, P., and K. Aki (1974). A precise, continuous measurement of seismic velocity for monitoring in situ stress, *J. Geophys. Res.* **79**, 399–406.
- Richter, T., C. Sens-Schönfelder, R. Kind, and G. Asch (2014). Comprehensive observation and modeling of earthquake and temperature-related seismic velocity changes in northern Chile with passive image interferometry, *J. Geophys. Res.* **119**, 4747–4765, doi: [10.1002/2013JB010695](https://doi.org/10.1002/2013JB010695).
- Schaff, D. P., and G. C. Beroza (2004). Coseismic and postseismic velocity changes measured by repeating earthquakes, *J. Geophys. Res.* **109**, no. B10, doi: [10.1029/2004JB003011](https://doi.org/10.1029/2004JB003011).
- Sens-Schönfelder, C., and U. Wegler (2006). Passive image interferometry and seasonal variations of seismic velocities at Merapi volcano, Indonesia, *Geophys. Res. Lett.* **33**, no. 21, L21302, doi: [10.1029/2006GL027797](https://doi.org/10.1029/2006GL027797).
- Snieder, R., A. Grêt, H. Douma, and J. Scales (2002). Coda wave interferometry for estimating nonlinear behavior in seismic velocity, *Science* **295**, 2253–2255, doi: [10.1126/science.1070015](https://doi.org/10.1126/science.1070015).
- Snieder, R., J. Sheiman, and R. Calvert (2006). Equivalence of the virtual-source method and wave-field deconvolution in seismic interferometry, *Phys. Rev. E.* **73**, no. 6, doi: [10.1103/PhysRevE.73.066620](https://doi.org/10.1103/PhysRevE.73.066620).
- Song, J., and H. Yang (2022). Seismic site response inferred from records at a dense linear array across the Chenghai fault zone, Binchuan, Yunnan, *J. Geophys. Res.* doi: [10.1029/2021JB022710](https://doi.org/10.1029/2021JB022710).

- Takano, T., T. Nishimura, H. Nakahara, Y. Ohta, and S. Tanaka (2014). Seismic velocity changes caused by the Earth tide: Ambient noise correlation analyses of small-array data, *Geophys. Res. Lett.* **41**, doi: [10.1002/2014GL060690](https://doi.org/10.1002/2014GL060690).
- Tsai, V. C. (2011). A model for seasonal changes in GPS positions and seismic wave speeds due to thermoelastic and hydrologic variations, *J. Geophys. Res.* **116**, no. B4, doi: [10.1029/2010JB008156](https://doi.org/10.1029/2010JB008156).
- Wang, B. S., H. K. Ge, W. Yang, W. T. Wang, B. Wang, G. H. Wu, and Y. J. Su (2012). Transmitting seismic station monitors fault zone at depth, *Eos Trans. AGU* **93**, no. 5, 49–50.
- Wang, B. S., W. Yang, W. T. Wang, J. Yang, X. B. Li, and B. Ye (2020). Diurnal and semidiurnal P- and S-wave velocity changes measured using an airgun source, *J. Geophys. Res.* **125**, e2019JB018218, doi: [10.1029/2019JB018218](https://doi.org/10.1029/2019JB018218).
- Wang, B. S., P. Zhu, Y. Chen, F. L. Niu, and B. Wang (2008). Continuous subsurface velocity measurement with coda wave interferometry, *J. Geophys. Res.* **113**, no. B12, doi: [10.1029/2007JB005023](https://doi.org/10.1029/2007JB005023).
- Wang, Q. Y., F. Brenguier, M. Campillo, A. Lecointre, T. Takeda, and Y. Aoki (2017). Seasonal crustal seismic velocity changes throughout Japan, *J. Geophys. Res.* doi: [10.1002/2017JB014307](https://doi.org/10.1002/2017JB014307).
- Wegler, U., B. G. Lühr, R. Snieder, and A. Ratdomopurbo (2006). Increase of shear wave velocity before the 1998 eruption of Merapi volcano (Indonesia), *Geophys. Res. Lett.* **33**, doi: [10.1029/2006GL025928](https://doi.org/10.1029/2006GL025928).
- Wessel, P., W. H. F. Smith, R. Scharroo, J. Luis, and F. Wobbe (2013). Generic mapping tools: Improved version released, *Eos Trans. AGU* **94**, 409–410.
- Winkler, K. W., and X. Liu (2005). Measurements of third-order elastic constants in rocks, *J. Acoust. Soc. Am.* **98**, 2886–2886.
- Yamamura, K., O. Sano, H. Utada, Y. Takei, S. Nakao, and Y. Fukao (2003). Long-term observation of *in situ* seismic velocity and attenuation, *J. Geophys. Res.* **108**, no. B6, doi: [10.1029/2002JB002005](https://doi.org/10.1029/2002JB002005).
- Yang, H., Y. Duan, J. Song, X. Jiang, X. Tian, W. Yang, W. Wang, and J. Yang (2020). Fine structure of the Chenghai fault zone, Yunnan, China, constrained from teleseismic travel time and ambient noise tomography, *J. Geophys. Res.* **125**, e2020JB019565, doi: [10.1029/2020JB019565](https://doi.org/10.1029/2020JB019565).
- Yang, H. F., Y. H. Duan, J. H. Song, W. T. Wang, W. Yang, X. F. Tian, and B. S. Wang (2021). Illuminating high-resolution crustal fault zones and temporal changes using multi-scale dense arrays and airgun sources, *Earthq. Res. Adv.* doi: [10.1016/j.eqrea.2021.100001](https://doi.org/10.1016/j.eqrea.2021.100001).
- Yang, H. F., Z. F. Li, Z. G. Peng, Y. Ben-Zion, and F. Vernon (2014). Low-velocity zones along the San Jacinto fault, southern California, from body waves recorded in dense linear arrays, *J. Geophys. Res.* **119**, doi: [10.1002/2014JB011548](https://doi.org/10.1002/2014JB011548).
- Yang, W., B. Wang, H. Ge, and S. Yuan (2018). Temporal variation of seismic wave velocity associated with groundwater level observed by downhole airgun near the Xiaojiang fault zone, *Seismol. Res. Lett.* doi: [10.1785/0220170282](https://doi.org/10.1785/0220170282).
- Zhang, Y., Y. An, F. Long, G. Zhu, M. Qin, Y. Zhong, Q. Xu, and H. Yang (2022). Short-term foreshock and aftershock patterns of the 2021 Ms 6.4 Yangbi earthquake sequence, *Seismol. Res. Lett.* doi: [10.1785/0220210154](https://doi.org/10.1785/0220210154).
- Zhu, G., H. Yang, Y. Tan, M. Jin, X. Li, and W. Yang (2022). The cascading foreshock sequence of the Ms 6.4 Yangbi earthquake in Yunnan, China, *Earth Planet. Sci. Lett.* doi: [10.1016/j.epsl.2022.117594](https://doi.org/10.1016/j.epsl.2022.117594).

Manuscript received 22 June 2022

Published online 7 March 2023